

# Quantifying the effect of ICME removal and observation age for in situ solar wind data assimilation

Harriet Turner<sup>1</sup>, Mathew J Owens<sup>1</sup>, Matthew Simon Lang<sup>1</sup>, Siegfried Gonzi<sup>2</sup>, and Pete Riley<sup>3</sup>

<sup>1</sup>University of Reading

<sup>2</sup>UK Met Office

<sup>3</sup>Predictive Science Inc.

November 26, 2022

## Abstract

Accurate space weather forecasting requires advanced knowledge of the solar wind conditions in near-Earth space. Data assimilation (DA) combines model output and observations to find an optimum estimation of reality and has led to large advances in terrestrial weather forecasting. It is now being applied to space weather forecasting. Here, we use solar wind DA with in-situ observations to reconstruct solar wind speed in the ecliptic plane between 30 solar radii and Earth's orbital radius. This is used to provide solar wind speed hindcasts. Here, we assimilate observations from the Solar Terrestrial Relations Observatory (STEREO) and the near-Earth dataset, OMNI. Analysis of two periods of time, one in solar minimum and one in solar maximum, reveals that assimilating observations from multiple spacecraft provides a more accurate forecast than using any one spacecraft individually. The age of the observations also has a significant impact on forecast error, whereby the mean absolute error (MAE) sharply increases by up to 23% when the forecast lead time first exceeds the corotation time associated with the longitudinal separation between the observing spacecraft and the forecast location. It was also found that removing coronal mass ejections from the DA input and verification time series reduces the forecast MAE by up to 10% as it removes false streams from the forecast time series. This work highlights the importance of an L5 space weather monitoring mission for near-Earth solar wind forecasting and suggests that an additional mission to L4 would further improve future solar wind DA forecasting capabilities.

1                   **Quantifying the effect of ICME removal and**  
2 **observation age for in situ solar wind data assimilation**

3                   **Harriet Turner<sup>1</sup>, Mathew Owens<sup>1</sup>, Matthew Lang<sup>1</sup>, Siegfried Gonzi<sup>2</sup>, Pete**  
4                   **Riley<sup>3</sup>**

5                   <sup>1</sup>Department of Meteorology, University of Reading, Earley Gate, PO Box 243, Reading, RG6 6BB, UK

6                   <sup>2</sup>Met Office, FitzRoy Road, Exeter, Devon, EX1 3PB, UK

7                   <sup>3</sup>Predictive Science Inc., 9990 Mesa Rim Rd., Suite 170, San Diego, CA92121, USA

8                   **Key Points:**

- 9                   • Assimilating in situ data from multiple spacecraft provides higher forecast skill  
10                   than from any one spacecraft individually.
- 11                   • The age of observations, in terms of time when the required Carrington longitude  
12                   was last observed, has a large effect on forecast skill.
- 13                   • Removing ICMEs from the assimilated time series provides a small increase in fore-  
14                   cast skill.

---

Corresponding author: Harriet Turner, [h.turner3@pgr.reading.ac.uk](mailto:h.turner3@pgr.reading.ac.uk)

## Abstract

Accurate space weather forecasting requires advanced knowledge of the solar wind conditions in near-Earth space. Data assimilation (DA) combines model output and observations to find an optimum estimation of reality and has led to large advances in terrestrial weather forecasting. It is now being applied to space weather forecasting. Here, we use solar wind DA with in-situ observations to reconstruct solar wind speed in the ecliptic plane between 30 solar radii and Earth’s orbital radius. This is used to provide solar wind speed hindcasts. Here, we assimilate observations from the Solar Terrestrial Relations Observatory (STEREO) and the near-Earth dataset, OMNI. Analysis of two periods of time, one in solar minimum and one in solar maximum, reveals that assimilating observations from multiple spacecraft provides a more accurate forecast than using any one spacecraft individually. The age of the observations also has a significant impact on forecast error, whereby the mean absolute error (MAE) sharply increases by up to 23% when the forecast lead time first exceeds the corotation time associated with the longitudinal separation between the observing spacecraft and the forecast location. It was also found that removing coronal mass ejections from the DA input and verification time series reduces the forecast MAE by up to 10% as it removes false streams from the forecast time series. This work highlights the importance of an L5 space weather monitoring mission for near-Earth solar wind forecasting and suggests that an additional mission to L4 would further improve future solar wind DA forecasting capabilities.

## Plain Language Summary

The effects of space weather can be damaging to technologies on Earth, potentially causing power outages and posing a hazard to humans in space. Accurate space weather forecasting requires advanced knowledge of the solar wind; a continual outflow of material from the Sun. Data assimilation (DA) is one method used in terrestrial weather forecasting, whereby model results are combined with observations to create an optimum estimation of reality. Here, we use a solar wind DA scheme to create 3 years of forecasts. It is found that assimilating observations from multiple spacecraft produces better forecasts than assimilating observations from a single spacecraft. It was also found that removing large eruptions, known as coronal mass ejections, from the DA input improves forecasts by reducing false alarms.

## 1 Introduction

The term “space weather” is used to describe the changing plasma conditions in the near-Earth space environment. It poses a threat to modern life through damaging technology, causing power failures and posing a risk to the health of humans in space (Cannon, 2013). For accurate space weather forecasting, advanced knowledge of the solar wind conditions is required. The solar wind is a continual stream of charged particles that flows from the high temperature corona (Parker, 1958). The most severe space weather events occur as a result of coronal mass ejections (CMEs), large eruptions of coronal plasma and magnetic field (Webb & Howard, 2012). CMEs have to propagate through the ambient solar wind, so it acts to modulate the severity of the CME and its impacts on Earth (Cargill, 2004; Case et al., 2008). Stream interaction regions (SIRs) are an inherent feature of the ambient solar wind and are caused by fast streams catching up with slower streams and creating regions of higher plasma density and stronger magnetic field (Gosling & Pizzo, 1999; Richardson & Cane, 2012). SIRs which persist for more than one solar rotation, are also referred to as corotating interaction regions (CIRs) and provide a source of recurring space weather.

Solar wind forecasting can be achieved through simple empirical methods, such as corotation (M. J. Owens et al., 2013; Kohutova et al., 2016; Thomas et al., 2018; Turner et al., 2021), or through more complex, physics-based approaches such as magneto-

65 hydrodynamic (MHD) models (Riley et al., 2001; Odstrcil, 2003; Tóth et al., 2005; Merkin  
66 et al., 2016). We here focus on improving the latter.

67 Data assimilation (DA) has led to large improvements in terrestrial weather fore-  
68 casting, but is yet to be fully utilised for space weather forecasting. DA combines prior  
69 information about a system (typically, from a numerical model) with observations to form  
70 an optimal estimation of reality, known as the posterior. Initial experiments into using  
71 DA for solar wind forecasting has shown potential for significant improvement in skill  
72 (Lang et al., 2017). The BRaVDA (Burger Radius Variational Data Assimilation) method-  
73 ology developed in Lang and Owens (2019) was subsequently used for producing hind-  
74 casts in Lang et al. (2021). BRaVDA uses a variational DA scheme (Dimet & Talagrand,  
75 1986; Lorenc, 1986), with the simplified solar wind model, HUX (Riley & Lionello, 2011).  
76 The output from BRaVDA was used to initialise a second reduced-physics solar wind  
77 propagation model, HUXt (M. Owens et al., 2020), though it could equally be used with  
78 MHD models too. Lang et al. (2021) showed that whilst the 27-day forecast root mean  
79 square error (RMSE) was comparable to that of corotation forecasts, it showed improve-  
80 ment over non-DA forecasts. To further investigate the performance of the BRaVDA scheme  
81 and perform a more rigorous analysis, we have increased the hindcast cadence from 27-  
82 days to 1-day, as this is how forecasts would be generated if a DA scheme were deployed  
83 operationally.

84 The BRaVDA scheme makes use of in situ observations of near-Earth solar wind  
85 conditions from the OMNI dataset (Vokhmyanin et al., 2019), and distant observations  
86 from the STEREO (Solar Terrestrial Relations Observatory) mission, which was launched  
87 in 2007 (Kaiser et al., 2008). The OMNI dataset uses solar wind observations from a suc-  
88 cession of spacecraft located at the L1 Lagrange point on the Sun-Earth line, at approx-  
89 imately 0.99AU. This is mostly comprised of observations from the *Wind* (Ogilvie et al.,  
90 1993; Lepping et al., 1995) and ACE (Advanced Composition Explorer; Stone et al. (1998))  
91 spacecraft propagated to the bow shock of Earth. The STEREO mission comprised of  
92 two spacecraft, STEREO-A and STEREO-B, which were placed into orbit around the  
93 Sun at approximately 1AU with STEREO-A ahead of Earth and STEREO-B behind.  
94 The spacecraft separate from Earth at approximately 22° per year and they passed be-  
95 hind the Sun in 2014. It was during this time that communication was lost with STEREO-  
96 B, and so the data used in this study is limited to STEREO-B’s operational lifetime be-  
97 tween 2007 and 2014.

98 The Lagrange points are gravitational nulls whereby the gravity of two large bod-  
99 ies balances the centripetal force of a smaller body. This means that spacecraft located  
100 at these positions will remain there, thus reducing the fuel required. There are five La-  
101 grange points, with L4 and L5 positioned 60 degrees ahead and behind Earth in its or-  
102 bit, respectively. A spacecraft located at either point would provide a near side-on view  
103 of the Sun-Earth line and so could provide remote-sensing observations of Earth-directed  
104 CMEs. Extensive studies have also shown the potential usefulness of an in situ space weather  
105 monitor at L5 [e.g. Akioka et al. (2005); Simunac et al. (2009)] and a mission is set for  
106 launch in 2027 (Davies, 2020). If this is joined by a space weather monitor at L4 (Posner  
107 et al., 2021), then these missions will provide additional observations that are useful for  
108 solar wind DA, as will be demonstrated in this study.

109 In this study, two analysis periods are used to assess the accuracy of hindcasts gen-  
110 erated using the BRaVDA scheme. The methods used in this study are described in Sec-  
111 tion 2, with BRaVDA methodology described in 2.1 and the forecast generation method  
112 in 2.2. The data assimilation experiments and their results are described in Section 3.  
113 Finally, we discuss implications and draw conclusions in Section 4.

## 2 Methods

### 2.1 BRaVDA scheme

The BRaVDA methodology was developed and extensively described in Lang and Owens (2019). The code is available at: <https://github.com/University-of-Reading-Space-Science/BRaVDA>. Here, we provide only a short overview of the methodology. BRaVDA is a variational DA scheme that incorporates in situ spacecraft observations of solar wind speed into the steady-state ‘‘HUX’’ solar wind model, based on Riley and Lionello (2011). Using the adjoint model of HUX, BRaVDA maps information contained within the in situ observations at 1 AU ( $\sim 215$  solar radii ( $R_S$ )) radially inwards to HUX’s inner boundary at  $30R_S$ . This information is then merged with a prior inner-boundary condition through the minimisation of a cost function comprised of the prior and observation errors weighted by their relative uncertainties. By finding the inner boundary condition that minimises this cost function, we find the solar wind speeds with the lowest errors respective of their relative uncertainties. This produces an updated inner boundary (the posterior state) which can be propagated radially outward by any solar wind model. For efficiency, we again use the HUX model, producing an optimal estimate of the true solar wind in the whole model domain, given the observations. The solar wind propagation model used in BRaVDA maps a 2 dimensional solar wind over the heliocentric domain from  $30R_S$  to  $236R_S$ .

The BRaVDA scheme requires that we define our prior state (our current estimate of the inner boundary condition), the prior error covariance matrix (a measure of the uncertainty present in our prior information) and the observation error covariance matrix (that gives a measure of the uncertainty in our observations relative to the HUX model).

We generate our ‘prior’ estimate of the solar wind speed at the inner boundary by using archived output of the HelioMAS model (data available from <https://www.predsci.com/portal/home.php>) at  $30R_S$ . HelioMAS is an MHD model that is initiated using radial magnetic field and solar wind speed derived from the coronal magnetic field topology (Riley et al., 2015) of the MAS (Magnetohydrodynamics Around a Sphere) model (Linker et al., 1999) solutions to the observed photospheric magnetic field. This prior state is then propagated out radially to  $236R_S$  with the HUX model to generate a prior estimate of the solar wind speed at Earth.

The prior error covariance matrix is estimated from an ensemble of HUX initial conditions (see Lang et al. (2017) for more details) generated by perturbing the HelioMAS  $30 R_S$  solution in the same manner as M. J. Owens and Riley (2017). The observation error covariance contains not only the measurement error, but also representivity errors that arise from the incorrect specification of observations in numerical models (such as errors from assuming the observations are on the model gridpoints, sub-grid processes etc.). An example of such a representivity error in the BRaVDA scheme is the fact that the HUX model is 2-dimensional, meaning that observations are always assumed to be at the heliographic latitude of Earth, whereas in reality observations away from Earth (such as provided by STEREO) may be at other heliographic latitudes. This representivity error is a large unknown at present and an area of ongoing research (Turner et al. (2021); M. J. Owens et al. (2020); Lang et al. (2021)). In this study, we use the same observation error covariance matrix as in Lang et al. (2021) to maintain consistency with previous work.

In this study, BRaVDA is run for two time periods; 01/08/2009 to 01/02/2011 and 01/04/2012 to 01/10/2013. These periods are highlighted in Figure 3. The earlier period covers the 18-months up to the separation between solar minimum and the rise to solar maximum, as described in Turner et al. (2021), and the later period is centred on solar maximum itself. This allows for analysis of solar wind forecasts in both phases of the solar cycle.

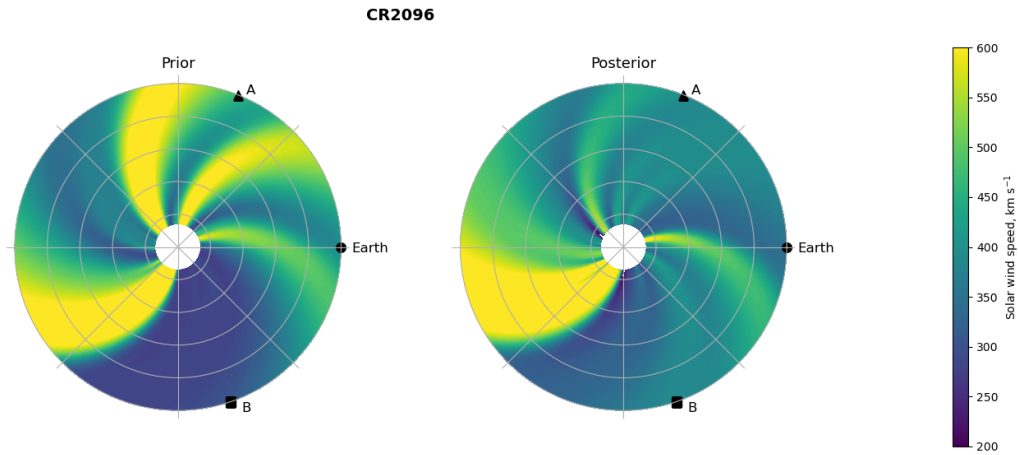


**Figure 1.** Solar wind solution from the HUX model initialised on 22/04/2010 for Carrington Rotation 2096 (22/04/2010 to 19/05/2010). The prior state (left) is that before the in situ data assimilation has taken place and the posterior state (right) is after the data assimilation. Indicated on both panels is the location of STEREO-A (A), Earth and STEREO-B (B) on 22/04/2010.

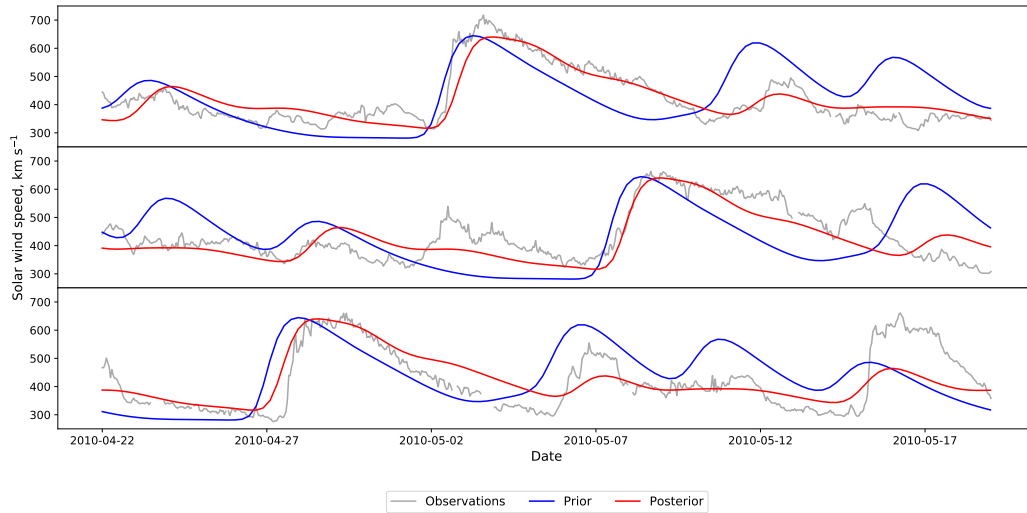


**Figure 2.** Time series at Earth's orbital distance of the solar wind solution for Carrington Rotation 2096 (22/04/2010 to 19/05/2010), as depicted in Figure 1. The top panel shows the solution at Earth, the middle panel at STEREO-A and the bottom panel at STEREO-B. The prior state is shown with the blue line, the posterior state with the red line and the grey line shows the observations taken from the respective spacecraft.

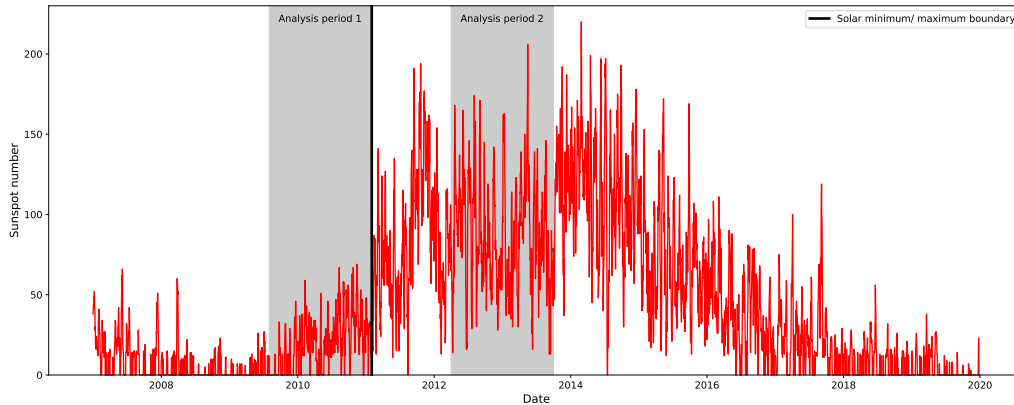


**Figure 3.** Evolution of sunspot number from 2007 to 2020. The analysis periods are highlighted in the grey shaded areas. The black vertical line shows the divide between solar minimum and solar maximum.

165        BRaVDA is run at daily cadence, using in situ observations which would have been  
 166        available at the time the forecast is performed, as in a genuine forecast. This expands  
 167        on the work in Lang et al. (2021), where BRaVDA was run every 27 days. The prior state  
 168        from HelioMAS, however, is only available as Carrington rotation solutions (i.e. every  
 169        27 days). In a true forecasting situation, the prior state would ideally be obtained from  
 170        daily-updated coronal solutions. However, the Carrington rotation solutions are adequate  
 171        for our purposes here, as the DA process makes significant changes to the prior state.  
 172        The likely effect of this is that the accuracy of the prior state is overestimated and the  
 173        forecast improvement from DA reduced from the value expected in an operational situ-  
 174        ation.

175        The output from each BRaVDA run gives a 27-day solar wind reconstruction from  
 176         $30R_S$  to  $215R_S$ , as shown in Figure 1. By taking the output from  $215R_S$ , this can be  
 177        used as a solar wind time series for Earth and the STEREO spacecraft, as shown in Fig-  
 178        ure 2.

## 179        2.2 Forecast generation

180        For each (daily) BRaVDA run, observations are assimilated from the previous 27  
 181        days up until the time the forecast is made,  $t_0$ . By assuming steady-state corotation of  
 182        the posterior solution, each BRaVDA run can be used to generate a single forecast with  
 183        a lead-time  $t_f$  of 0 to 27 days with respect to  $t_0$ . An example is shown in Figure 4. The  
 184        single BRaVDA run produces a single solar wind speed estimate at each forecast lead  
 185        time from 0 to 27 days. As BRaVDA is run on a daily cadence, a forecast time series  
 186        for a particular lead time, e.g.  $t_f = 5$  days, at a given location can be created by com-  
 187        bining forecasts for different  $t_0$ . While forecasts can be generated for the whole model  
 188        domain, from  $30 R_S$  out to  $215 R_S$  and for all longitudes, here we only consider the lo-  
 189        cations of STEREO-A, STEREO-B and OMNI.

190        For the periods of time used in the analysis here, the spacecraft separation, and  
 191        therefore corotation time between observation and Earth, changes over the analysis pe-  
 192        riod (see Table 1).

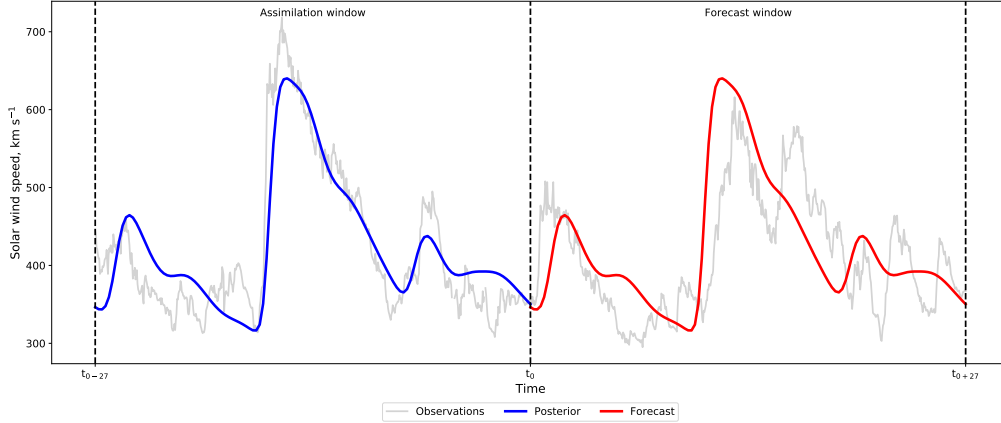


**Figure 4.** Using BRaVDA posterior output (blue) as a solar wind speed forecast (red).  $t_0$  is the start of the forecast window, which is here 27 days long. It is also the end of the assimilation window, wherein observations from the previous 27 days up until  $t_0$  are assimilated. The solar wind observations for this period are shown in grey.

| Date       | Spacecraft corotation time [days] |              |              |              |            |            |
|------------|-----------------------------------|--------------|--------------|--------------|------------|------------|
|            | Earth to STA                      | STA to Earth | STB to Earth | Earth to STB | STB to STA | STA to STB |
| 01/08/2009 | 4.3                               | 22.7         | 3.7          | 23.3         | 8.0        | 18.9       |
| 01/02/2011 | 6.5                               | 20.5         | 6.9          | 20.1         | 13.4       | 13.6       |
| 01/04/2012 | 8.3                               | 18.7         | 8.9          | 18.1         | 17.2       | 9.8        |
| 01/10/2013 | 11.0                              | 16.0         | 10.5         | 16.5         | 21.5       | 5.5        |

**Table 1.** Corotation time for the different spacecraft pairings, taking into account only the spacecraft longitudinal separation. The dates are the starts and ends of the solar minimum and solar maximum intervals.

### 3 Data assimilation experiments and results

Throughout this study we consider the variation of forecast mean absolute error (MAE) with forecast lead time. Here we describe a number of individual BRaVDA experiments aimed at diagnosing specific aspects of forecast MAE.

#### 3.1 Forecast lead time

We first look at the effect of forecast lead time on MAE. For this, we assimilate observations from all three spacecraft (OMNI, STEREO-A and STEREO-B) and the output from BRaVDA is used to create forecasts at the locations of Earth, STEREO-A and STEREO-B for lead times of 0 to 27 days. This is done for both solar minimum and solar maximum time intervals. Figure 5 shows the MAE between the forecast and observed solar wind speed for a range of forecast lead times. As forecast lead time increases, there is a general trend for increasing forecast MAE. The left-hand panel shows the solar minimum interval, where MAE is generally lower than the solar maximum interval, shown in the right-hand panel. This is true for all three forecast locations. Note, however, that spacecraft separation (in solar longitude and latitude) also increases between these two time periods, so the difference in MAE between the solar minimum and maximum intervals cannot necessarily be attributed to the solar cycle.

#### 3.2 Assimilation of individual spacecraft and age of observations

We now consider the effect of assimilating different combinations of spacecraft. Experiments were carried out assimilating observations from all spacecraft together, as above, and assimilating the spacecraft observations individually. Figure 6 shows the MAE variation with forecast lead time for these different experiments. Here, the forecasts at Earth location are in the top row, at STEREO-A in the second row and at STEREO-B in the bottom row. The solar minimum interval is in the left-hand column and solar maximum in the right-hand column.

The most obvious trend is that assimilating all spacecraft produces a forecast with the lower MAE than any one spacecraft individually. This is true at all locations and for all non-zero lead times. The exception is for very long lead-time forecasts ( $> 20$  days) at STEREO-B, where the MAE for assimilating all spacecraft is comparable to assimilating only STEREO-B data.

Overall, there is still a general trend of increasing MAE with lead time. When all spacecraft are assimilated, the MAE increase with lead time is fairly smooth, if not necessarily linear. When looking at the assimilation of individual spacecraft, however, there are clear step changes in MAE with forecast lead time. These can be understood in terms of the corotation time.

When only individual spacecraft are assimilated, the lowest MAE at short, non-zero forecast lead times (e.g.  $< 5$  days) is obtained when assimilating the spacecraft ‘ahead’ (in terms of solar rotation, meaning at lower Carrington longitude) of the forecast location. This can be seen in Figure 6; for example, the forecast MAE at STEREO-A’s location (middle row) when assimilating only near-Earth observations (blue line) is initially below that obtained when assimilating only STEREO-A (orange line) or STEREO-B (red line). This remains the case for forecast lead times out to 5 days during the solar minimum period, and 10 days for the solar maximum period. Between these two time periods, STEREO-A separates from Earth, increasing from 57 to 87 degrees ahead. Thus observations at Earth provide recent information at STEREO-A for up to 5 and 10 days. The other panels show similar transitions are associated with the forecast lead time exceeding the corotation time.

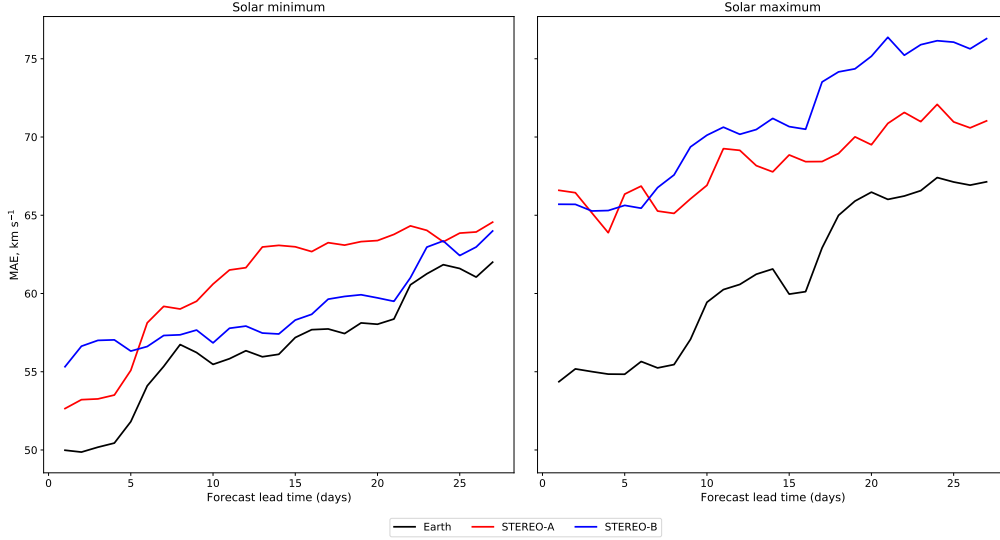


**Figure 5.** Mean absolute error (MAE) of solar wind forecasts as a function of forecast lead time, for the case where all spacecraft observations are assimilated. The forecast at Earth location is shown in black, at STEREO-A in red and at STEREO-B in blue. The solar minimum interval (01/08/2009 to 01/02/2011) is in the left-hand panel and the solar maximum interval (01/04/2012 to 01/10/2013) in the right-hand panel.

| Assimilated spacecraft | Forecast location | MAE [km/s] |       |        |           |       |        |
|------------------------|-------------------|------------|-------|--------|-----------|-------|--------|
|                        |                   | 2009-2011  |       |        | 2012-2013 |       |        |
|                        |                   | Before     | After | % diff | Before    | After | % diff |
| OMNI                   | Earth             | -          | -     | -      | -         | -     | -      |
|                        | STEREO-A          | 57.8       | 71.2  | 23.2   | 68.7      | 82.0  | 19.4   |
|                        | STEREO-B          | 66.1       | 74.5  | 12.7   | 74.5      | 91.7  | 23.1   |
| STEREO-A               | Earth             | 58.8       | 71.2  | 21.1   | 68.8      | 78.7  | 14.4   |
|                        | STEREO-A          | -          | -     | -      | -         | -     | -      |
|                        | STEREO-B          | 67.6       | 73.7  | 9.0    | 67.3      | 79.8  | 18.6   |
| STEREO-B               | Earth             | 57.0       | 69.6  | 22.1   | 63.4      | 74.2  | 17.0   |
|                        | STEREO-A          | 67.3       | 73.0  | 8.5    | 73.6      | 81.1  | 10.2   |
|                        | STEREO-B          | -          | -     | -      | -         | -     | -      |

**Table 2.** Forecast MAE for different time intervals, different locations and different assimilated spacecraft. Before and After indicate forecasts where the lead time is less than or greater than the minimum corotation time between assimilated spacecraft and forecast location, respectively. Where it is left blank, this is because the lead time never exceeds the corotation time.

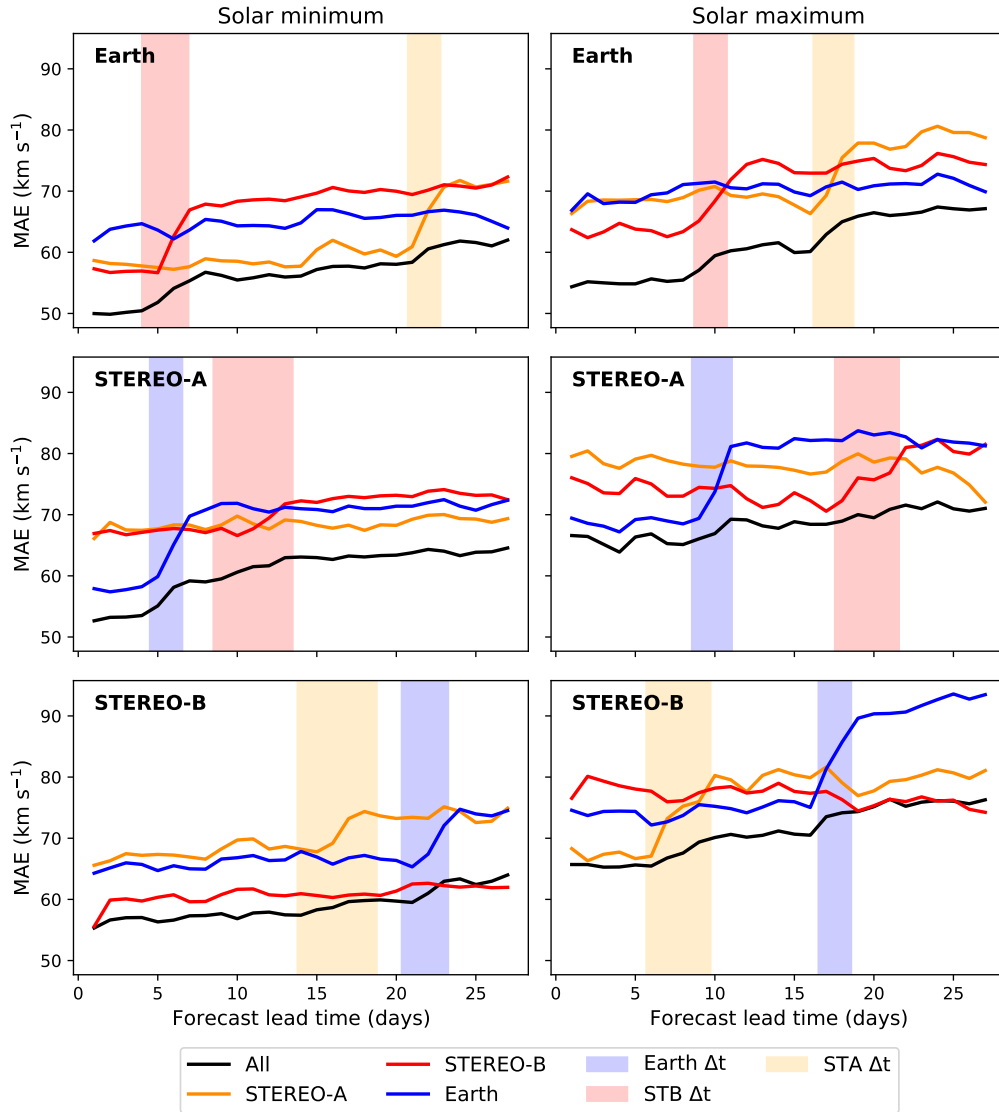


**Figure 6.** Mean absolute error of solar wind forecasts as a function of forecast lead time, for different combinations of assimilated spacecraft (coloured lines, as indicated by the legend) and different forecast locations (rows of panels). The left hand column is the solar minimum interval, from 01/08/2009 to 01/02/2011, and the right hand column is the solar maximum interval, 01/04/2012 to 01/10/2013. The shaded regions show the corotation time from the spacecraft indicated by colour (blue for Earth, yellow for STEREO-A and red for STEREO-B) to the forecast location.

240 Table 2 shows the average MAE separated into intervals before and after when the  
 241 lead time is less than or greater than the minimum corotation time between assimilated  
 242 spacecraft and forecast location. For all assimilated spacecraft and forecast locations,  
 243 there is an increase in MAE of between 8.5 and 23.2%, with an average value of 16.6%.  
 244 Of course, increased lead time is expected to result in increased MAE, regardless of corota-  
 245 tion time. But Figure 6 shows that this trend is much smaller, typically of the order  
 246 a few percent.

247 The large jumps in MAE are due to the age of the observations, whereby once the  
 248 forecast lead time ( $t_f$ ) exceeds the corotation time ( $t_C$ ), observations from the previous  
 249 Carrington rotation are being used. This means that the effective age of observations  
 250 ( $\tau$ ) for  $t_f > t_C$  is  $t_f + 27$  days. For example, when assimilating only STEREO-B and  
 251 forecasting at Earth, as Table 1 shows, the corotation time increases from 3.7 to 6.9 days  
 252 over the 01/08/2009 to 01/02/2011 period. Therefore, as lead times exceed  $\sim 5$  days,  
 253 we expect an increase in MAE as  $\tau$  jumps from  $\tau < 6.9$  to  $\tau > 30.7$ . This can be seen  
 254 in Figure 6, where the red shaded region in the top left plot shows the corotation time  
 255 for STEREO-B to Earth for that period. This effect can be seen in a number of other  
 256 situations where single spacecraft are assimilated. When assimilating multiple spacecraft,  
 257 the abrupt change in age of observation effect is lessened; although there is an increase  
 258 in the forecast error over the shaded regions of Figure 6, the curve is not as steep as when  
 259 assimilating only the spacecraft associated with that corotation time. Therefore, assim-  
 260 ilating multiple spacecraft reduces the effect of the age of observations impacting the fore-  
 261 cast MAE.

### 262 3.3 Removal of ICMEs

263 The interplanetary manifestations of CMEs (ICMEs) provide a potential source of  
 264 error for forecasts using the DA output. For example, if a fast ICME encounters one of  
 265 the assimilated spacecraft during the assimilation window, the ICME will be reconstructed  
 266 in the output as if it were time-stationary fast solar wind stream. When this output is  
 267 subsequently used for forecasting, it would produce a false fast stream in the forecast time  
 268 series. Therefore, by removing ICMEs from the input time series of all spacecraft, the  
 269 production of the false streams in the forecast time series can potentially be prevented.

270 Conversely, if a fast ICME encounters the forecast location during the forecast win-  
 271 dow, the forecast will miss the transient fast stream, as there will have been no corre-  
 272 sponding fast stream in the assimilation window. Thus removing ICMEs from the ver-  
 273 ification time series allows us to better assess how well BRaVDA is reproducing the am-  
 274 bient solar wind structure, without penalising for missing transient ICME structures, which  
 275 it is not expected to capture. (However, note that accurate reconstruction of the am-  
 276 bient solar wind is required to produce accurate ICME arrival time forecasts (e.g. Case  
 277 et al. (2008)). Thus we present results of removing ICMEs from the DA-input time se-  
 278 ries, the verification time series, and both. Times associated with ICMEs are identified  
 279 using the HELCATS ICME list (Möstl et al., 2022). To ensure all of the disturbance as-  
 280 sociated with the ICME is removed, we eliminate 24 hours either side of the ICME lead-  
 281 ing disturbance and ICME trailing edge times. For the purposes of assimilated data, the  
 282 data gap produced by removing an ICME is then linearly interpolated over to make a  
 283 complete time series. Qualitatively similar results are obtained by simply removing times  
 284 identified as ICMEs.

285 An example of the effect of removing ICMEs is shown in Figure 7. A fast ICME  
 286 (maximum of  $720 \text{ km s}^{-1}$ ) was identified at STEREO-B, seen as an isolated velocity spike  
 287 between 22/09/2012 to 29/09/2012. This ICME was removed from the STEREO-B in-  
 288 put and linearly interpolated to give the green line in the top panel of Figure 7. The bot-  
 289 tom three panels show 5-day forecasts at Earth, STEREO-A and STEREO-B with (solid  
 290 lines) and without (dashed lines) the ICME present in the assimilated STEREO-B time

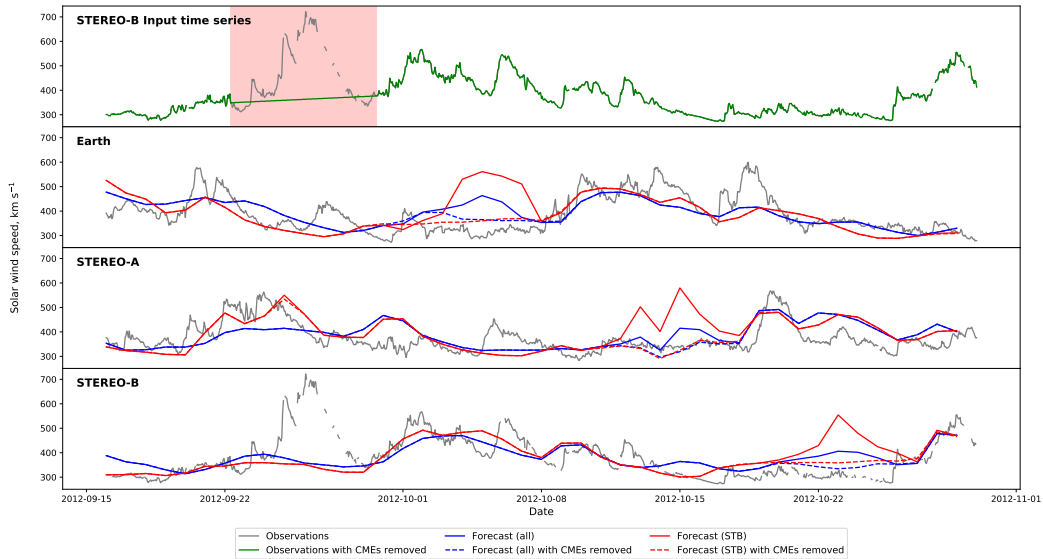


**Figure 7.** Time series of; top panel, the STEREO-B observations with the ICME included (grey) and with it removed (green); second panel, forecast with 5-day lead time for Earth; third panel, forecast with 5-day lead time for STEREO-A; bottom panel, forecast with 5-day lead time for STEREO-B. The blue lines show when all spacecraft observations are assimilated and the red lines show only STEREO-B observations assimilated. The solid line shows when the ICME is included in the STEREO-B input series and the dashed line when the ICME is removed. The red shaded region in the top panel shows the time span of the ICME plus 24 hours either side.

291 series. Red lines show assimilation of STEREO-B data only, while blue lines show as-  
 292 simulation of all three spacecraft data.

293 It can be seen that removing the ICME causes an improvement in the forecast, by  
 294 removing a false fast stream, a certain time later. The time delay from ICME removal  
 295 to forecast improvement relates to the corotation time between the spacecraft, which is  
 296 determined by their longitudinal separation. At this time, the corotation time from STEREO-  
 297 B to Earth is approximately 9 days, STEREO-B to STEREO-A is approximately 18 days  
 298 and the full Carrington rotation to STEREO-B is 27 days. It is after these respective  
 299 times from the ICME that the improvement is seen in the forecast for that spacecraft.  
 300 Furthermore, Figure 7 shows even without removal of ICMEs from the assimilation data  
 301 (which may be difficult in real-time operational forecasting), assimilating multiple space-  
 302 craft observations reduces the magnitude of the false fast stream that is present in the  
 303 forecasts following. Comparing the red and blue solid lines, when all spacecraft obser-  
 304 vations are assimilated, the false stream magnitude is reduced by approximately  $150 \text{ km s}^{-1}$   
 305 in the forecasts.

306 Figure 8 shows the variation of forecast MAE with forecast lead times for combi-  
 307 nations of ICME removal from the DA input time series and the verification time series.  
 308 There are four combinations; ICMEs remaining in both time series, ICMEs removed from  
 309 the input time series but remaining in the verification time series, ICMEs remaining in  
 310 the input time series but removed from the verification time series and ICMEs removed  
 311 from both time series. It can be seen from Figure 8 and from the average MAE values  
 312 in Table 3 that, generally, removing ICMEs leads to forecast improvement. For exam-  
 313 ple, for the forecast at Earth, the average MAE across all lead times is  $56.1$  and  $60.7 \text{ km s}^{-1}$   
 314  $\text{s}^{-1}$  for the solar minimum and solar maximum intervals respectively. By removing ICMEs

| ICMEs in input? | ICMEs in verification? | Solar minimum |      |      | Solar maximum |      |      |
|-----------------|------------------------|---------------|------|------|---------------|------|------|
|                 |                        | Earth         | STA  | STB  | Earth         | STA  | STB  |
| Yes             | Yes                    | 56.1          | 60.3 | 58.7 | 60.7          | 68.1 | 70.7 |
|                 | No                     | 55.2          | 59.8 | 57.8 | 60.8          | 63.1 | 65.6 |
| No              | Yes                    | 55.9          | 60.4 | 58.4 | 60.0          | 66.9 | 68.4 |
|                 | No                     | 55.1          | 59.6 | 57.5 | 59.5          | 61.9 | 63.1 |

**Table 3.** Average forecast MAE (over all lead times) for combinations of removing ICMEs from the DA input time series and the verification time series. The average MAE is shown for both the solar minimum (01/08/2009 to 01/02/2011) and solar maximum (01/04/2012 to 01/10/2013) intervals. Top row: ICMEs are included in both the DA input and verification time series. Second row: ICMEs are included in the DA input time series and removed from the verification time series. Third row: ICMEs are removed from the DA input time series and remain in the verification time series. Bottom row: ICMEs are removed from both the DA input and verification time series.

| ICMEs in input? | ICMEs in verification? | Solar minimum |      |      | Solar maximum |      |       |
|-----------------|------------------------|---------------|------|------|---------------|------|-------|
|                 |                        | Earth         | STA  | STB  | Earth         | STA  | STB   |
| Yes             | No                     | -1.6          | -0.8 | -1.5 | 0.2           | -7.3 | -7.2  |
| No              | Yes                    | -0.4          | 0.2  | -0.5 | -1.2          | -1.8 | -3.3  |
|                 | No                     | -1.8          | -1.2 | -2.0 | -2.0          | -9.1 | -10.7 |

**Table 4.** Percentage difference of the average MAE for forecasts (over all lead times) with combinations of ICMEs removed from the DA input time series and verification time series compared with the forecasts where ICMEs remain. Where the difference is negative, this indicates the average MAE without ICMEs is smaller than with ICMEs included. Top row: ICMEs remain in the DA input time series and are removed from the verification time series. Middle row: ICMEs are removed from the DA time series and remain in the verification time series. Bottom row: ICMEs are removed from both the DA input and verification time series.

315 from both the input and verification time series, these are reduced to 55.1 km s<sup>-1</sup> for  
316 solar minimum and 59.5 km s<sup>-1</sup> for solar minimum, which is as percentage difference of  
317 -1.8% and -2.0% respectively, as shown in Table 4. There is greater improvement in the  
318 solar maximum period, particularly at STEREO-A and STEREO-B. This is due to a larger  
319 number of ICMEs at this time, with a total number of 72 ICMEs observed during the  
320 solar minimum period compared to 138 during the solar maximum period. We further  
321 classify fast ICMEs as those with an average proton speed of more than 500 km s<sup>-1</sup>, as  
322 taken from the HELCATS ICME catalogue. 20 fast ICMEs were observed during the  
323 solar maximum period and 6 during the solar minimum period. Out of the 20 fast ICMEs  
324 during the solar maximum period, 5 of these were at Earth, 7 at STEREO-A and 8 at  
325 STEREO-B. Although only a small difference between the spacecraft, this could account  
326 for the -2.0% difference at Earth compared with the -9.1% at STEREO-A and -10.7%  
327 at STEREO-B.

## 328 4 Discussion and conclusions

329 In this study we have performed a number of solar wind data assimilation exper-  
330 iments to determine how forecast error is expected to vary with a number of different

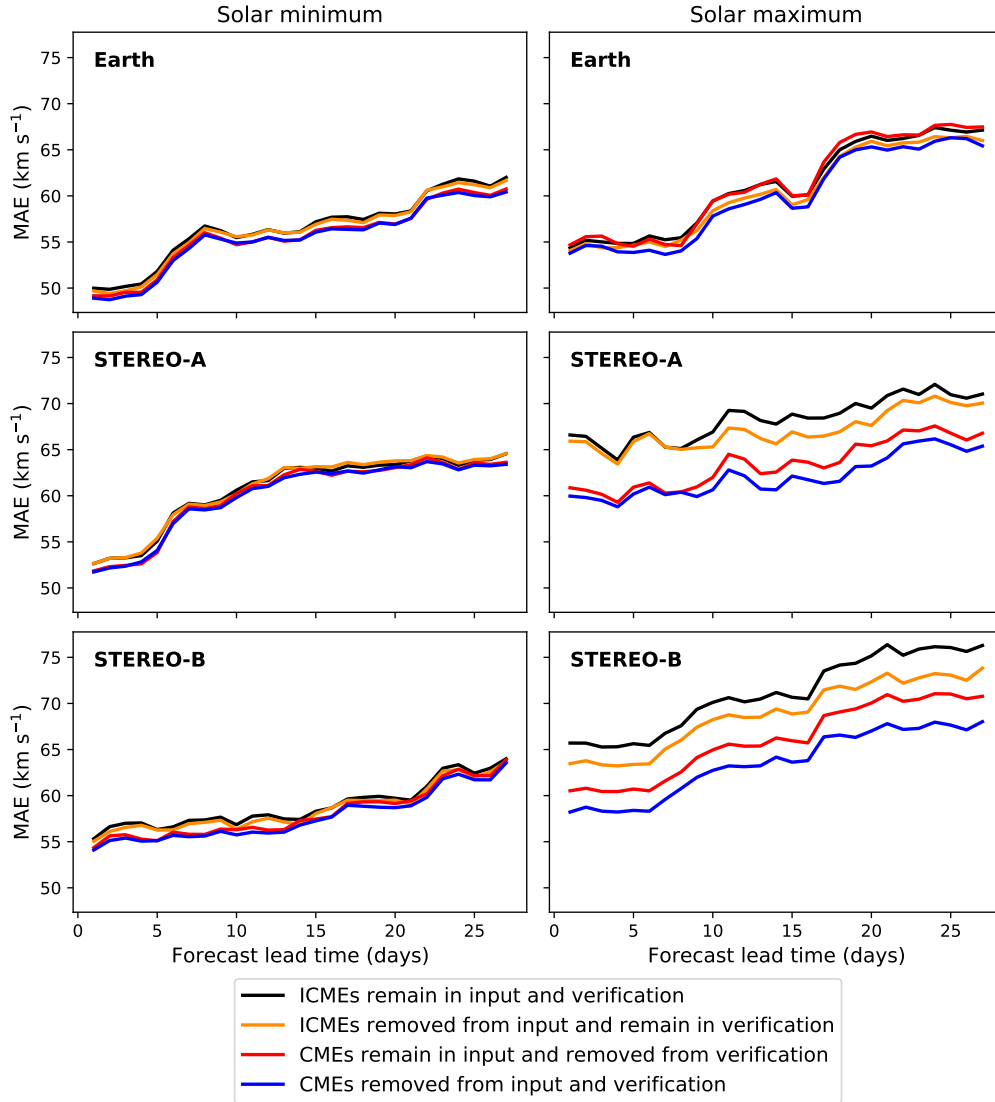


**Figure 8.** Variation of forecast MAE with forecast lead time for different combinations of ICME removal from the input and verification time series. The black line shows the case when the ICMEs remain in both DA input and verification time series. The red line shows the case when ICMEs are removed from the verification time series only. The orange line shows the case when ICMEs are removed from the DA input series only. The blue line shows the case when ICMEs are removed from both the DA input and verification time series. All spacecraft are assimilated in all cases.

331 factors. Here, mean absolute error (MAE) was used as the metric to analyse the fore-  
 332 cast accuracy. Although MAE is a single metric and it can sometimes mislead (M. J. Owens,  
 333 2018), it is useful here as the individual changes to the DA process that we are testing  
 334 produce time series that are, for the most part, qualitatively similar. Future work will  
 335 focus on a more complete analysis of forecast performance.

336 We have shown that assimilating observations from multiple spacecraft produces  
 337 a forecast with lower MAE than when assimilating observations from any one single space-  
 338 craft. This is despite the fact that observations may not be ideally placed, due to the  
 339 inclination of the ecliptic plane to the solar equator (M. J. Owens et al., 2019, 2020). As-  
 340 similation of the STEREO spacecraft observations, along with OMNI, has shown to im-  
 341 prove forecasts and so the addition of space weather monitors at both L4 and L5 can only  
 342 aid future development of solar wind DA. This stresses the value of multiple, well sep-  
 343 arated, space weather monitoring missions, such as at the L5 point (Lagrange mission,  
 344 Davies (2020)), but also the importance of a mission to the L4 point (see Posner et al.  
 345 (2021)).

346 The “age” of the observations, in terms of the time since a Carrington longitude  
 347 was last observed by a particular spacecraft, also has a large effect on forecast error. When  
 348 assimilating data from a single spacecraft, there is a large increase in MAE once the fore-  
 349 cast lead time is greater than the corotation time from that spacecraft to the forecast  
 350 location. This is due to the assumption of steady state conditions becoming increasingly  
 351 less valid. Although assimilating multiple spacecraft does not completely remove this ef-  
 352 fect, it is greatly reduced and the discontinuous increases in MAE with forecast lead time  
 353 are reduced. But further forecast improvement may be obtained by weighting observa-  
 354 tions by their age. Simple experiments testing this idea with BRaVDA (not shown) have  
 355 been inconclusive. However, as BRaVDA is based upon HUX (Riley & Lionello, 2011),  
 356 which is not time dependent, it is not easy to explicitly implement this. Future exper-  
 357 iments using the time-dependent version of HUX (M. Owens et al., 2020, HUXt) are planned.

358 ICMEs have the potential to introduce false streams into the BRaVDA output, lead-  
 359 ing to false alarms in the forecasts. As ICMEs are transient events rather than corotat-  
 360 ing solar wind streams, they are not correctly captured in BRaVDA. If a fast ICME en-  
 361 counters one of the assimilating spacecraft, it will be treated as a fast ambient solar wind  
 362 stream and assumed to persist at the observed Carrington longitude. Thus a fast stream  
 363 is subsequently incorrectly forecast. This was demonstrated when considering a single  
 364 fast ICME encountered by STEREO-B in late September 2012. This ICME was removed  
 365 from the input observations at STEREO-B and the resulting BRaVDA output was used  
 366 for forecasting at Earth, STEREO-A and STEREO-B. There was a marked improvement  
 367 in the 5-day lead time forecast time series at Earth, STEREO-A and STEREO-B, through  
 368 reduction of a region of forecast high solar wind. This was seen for the cases where only  
 369 STEREO-B observations were assimilated and when all three spacecraft observations were  
 370 assimilated. When only the STEREO-B observations were assimilated, the false fast stream  
 371 appeared larger in the forecast time series than when all spacecraft observations were  
 372 assimilated, as the ICME was only observed at one spacecraft. Although assimilation  
 373 of multiple observations caused this false alarm to be of a lower magnitude than the fast  
 374 ICME in the observations, it did not completely remove it.

375 More generally applying the ICME removal to the solar minimum and solar max-  
 376 imum time periods showed a general improvement in the forecast accuracy. However, im-  
 377 provements were modest, as all three spacecraft were assimilated, which already reduces  
 378 the effect of transient ICMEs.

379 The largest improvement in the solar maximum period at STEREO-A and STEREO-  
 380 B, due to the larger number of fast ICMEs observed at these spacecraft. It was found  
 381 that removing ICMEs from the verification time series caused a larger improvement in  
 382 the forecast MAE than removing them from the DA input time series. This is due to BRaVDA

383 missing fast streams having a larger effect than creating fast streams through misinter-  
 384 preting an ICME. As an ICME would be observed at only one spacecraft, assimilating  
 385 multiple observations limits the reconstruction of the ICME as a steady-state solar wind  
 386 structure, thus reducing the production of a false alarm in the forecast. For BRaVDA  
 387 to be deployed operationally, an algorithm to automatically detect and remove ICMEs  
 388 from the real time solar wind data would be required. Some methods based on proton  
 389 temperature (Cane & Richardson, 2003) and iron charge state have been tested with coro-  
 390 rotation forecasts (Kohutova et al., 2016). Removing ICMEs using these indicators led to  
 391 an improvement in forecast skill score, so this technique could be applied for operational  
 392 DA. Developing BRaVDA for operational solar wind forecasting will additionally require  
 393 the use of real-time spacecraft observations, analysis of which is left for future work.

#### 394 Acknowledgments

395 OMNI data were downloaded from the OMNIWeb portal at <https://omniweb.gsfc.nasa.gov/ow.html>. STEREO-A and STEREO-B data were downloaded from the CDAWeb  
 396 Data Explorer portal at <https://cdaweb.gsfc.nasa.gov/>. Spacecraft location data were  
 397 downloaded from <https://omniweb.gsfc.nasa.gov/coho/helios/heli.html>. HelioMAS  
 398 model output is available from the Predictive Science Inc. (website: <http://www.predsci.com/mhdweb/home.php>). Harriet Turner is funded through SCENARIO grant number  
 399 NE/S007261/1. Work was part-funded by Science and Technology Facilities Council (STFC)  
 400 grant numbers ST/R000921/1 and ST/V000497/1, and Natural Environment Research  
 401 Council (NERC) grant number NE/S010033/1.  
 402  
 403

#### 404 References

- 405 Akioka, M., Nagatsuma, T., Miyake, W., Ohtaka, K., & Marubashi, K. (2005). The  
 406 L5 mission for space weather forecasting. *Advances in Space Research*, *35*(1),  
 407 65–69. doi: 10.1016/j.asr.2004.09.014
- 408 Cane, H. V., & Richardson, I. G. (2003). Interplanetary coronal mass ejections in  
 409 the near-Earth solar wind during 1996–2002. *Journal of Geophysical Research: Space Physics*, *108*(A4). doi: 10.1029/2002JA009817
- 410 Cannon, P. S. (2013). Extreme space weather - A report published by the UK royal  
 411 academy of engineering. *Space Weather*, *11*(4), 138–139. doi: 10.1002/swe  
 412 .20032
- 413 Cargill, P. J. (2004). On the aerodynamic drag force acting on interplanetary coro-  
 414 nal mass ejections. *Solar Physics*, *221*(1), 135–149. doi: 10.1023/B:SOLA  
 415 .0000033366.10725.a2
- 416 Case, A. W., Spence, H. E., Owens, M. J., Riley, P., & Odstrcil, D. (2008). Am-  
 417 bient solar winds’ effect on ICME transit times. *Geophysical Research Letters*,  
 418 *35*(15), 1–5. doi: 10.1029/2008GL034493
- 419 Davies, J. (2020). The COR and HI Instruments for the Lagrange L5 Mission. In  
 420 *The cor and hi instruments for the lagrange l5 mission*.
- 421 Dimet, F. L., & Talagrand, O. (1986). Variational algorithms for analysis and assim-  
 422 ilation of meteorological observations: theoretical aspects. *Tellus A*, *38* A(2),  
 423 97–110. doi: 10.1111/j.1600-0870.1986.tb00459.x
- 424 Gosling, J. T., & Pizzo, V. J. (1999). Formation and Evolution of Corotating In-  
 425 teraction Regions and Their Three Dimensional Structure. *Space Science Re-  
 426 views*, *89*, 21–52. doi: 10.1007/978-94-017-1179-1.3
- 427 Kaiser, M. L., Kucera, T. A., Davila, J. M., Cyr, O. C., Guhathakurta, M., & Chris-  
 428 tian, E. (2008). The STEREO mission: An introduction. *Space Science  
 429 Reviews*, *136*(1-4), 5–16. doi: 10.1007/s11214-007-9277-0
- 430 Kohutova, P., Bocquet, F. X., Henley, E. M., & Owens, M. J. (2016). Improving  
 431 solar wind persistence forecasts: Removing transient space weather events,  
 432 and using observations away from the Sun-Earth line. *Space Weather*, *14*(10),  
 433

- 802–818. doi: 10.1002/2016SW001447
- Lang, M., Browne, P., van Leeuwen, P. J., & Owens, M. (2017). Data Assimilation in the Solar Wind: Challenges and First Results. *Space Weather*, *15*(11), 1490–1510. doi: 10.1002/2017SW001681
- Lang, M., & Owens, M. J. (2019). A Variational Approach to Data Assimilation in the Solar Wind. *Space Weather*, *17*(1), 59–83. doi: 10.1029/2018SW001857
- Lang, M., Witherington, J., Owens, M. J., & Turner, H. (2021). Improving solar wind forecasting using Data Assimilation. *Space Weather*, 1–23.
- Lepping, R. P., Acuña, M. H., Burlaga, L. F., Farrell, W. M., Slavin, J. A., Schatten, K. H., ... Worley, E. M. (1995). The WIND magnetic field investigation. *Space Science Reviews*, *71*(1-4), 207–229. doi: 10.1007/BF00751330
- Linker, J. A., Mikić, Z., Biesecker, D. A., Forsyth, R. J., Gibson, S. E., Lazarus, A. J., ... Thompson, B. J. (1999, may). Magnetohydrodynamic modeling of the solar corona during Whole Sun Month. *Journal of Geophysical Research: Space Physics*, *104*(A5), 9809–9830. Retrieved from <https://onlinelibrary.wiley.com/doi/10.1029/1998JA900159> doi: 10.1029/1998JA900159
- Lorenc, A. C. (1986). Analysis methods for numerical weather prediction. *Quarterly Journal of the Royal Meteorological Society*, *112*(474), 1177–1194. doi: 10.1002/qj.49711247414
- Merkin, V. G., Lyon, J. G., Lario, D., Arge, C. N., & Henney, C. J. (2016). Time-dependent magnetohydrodynamic simulations of the inner heliosphere. *Journal of Geophysical Research A: Space Physics*, *121*(4), 2866–2890. doi: 10.1002/2015JA022200
- Möstl, C., Boakes, P., Isavnin, A., Kilpua, E. K., Winslow, R., Anderson, B., ... Eastwood, J. (2022). *HELcats WP4 Catalogue*. Retrieved from [https://www.helcats-fp7.eu/catalogues/wp4{\\\_}icmecat.html](https://www.helcats-fp7.eu/catalogues/wp4{\_}icmecat.html) doi: 10.6084/m9.figshare.4588315.v1
- Odstroil, D. (2003). Modeling 3-D solar wind structure. *Advances in Space Research*, *32*(4), 497–506. doi: 10.1016/S0273-1177(03)00332-6
- Ogilvie, K. W., Chornay, D. J., Fritzenreiter, R. J., Hunsaker, F., Keller, J., Lobell, J., ... Gergin, E. (1993). Swe, a comprehensive plasma instrument for the wind spacecraft. *Space Science Reviews*, *8*(71), 55–77.
- Owens, M., Lang, M., Barnard, L., Riley, P., Ben-Nun, M., Scott, C. J., ... Gonzi, S. (2020). A Computationally Efficient, Time-Dependent Model of the Solar Wind for Use as a Surrogate to Three-Dimensional Numerical Magnetohydrodynamic Simulations. *Solar Physics*, *295*(3). Retrieved from <http://dx.doi.org/10.1007/s11207-020-01605-3> doi: 10.1007/s11207-020-01605-3
- Owens, M. J. (2018). Time-Window Approaches to Space-Weather Forecast Metrics: A Solar Wind Case Study. *Space Weather*, *16*(11), 1847–1861. doi: 10.1029/2018SW002059
- Owens, M. J., Challen, R., Methven, J., Henley, E., & Jackson, D. R. (2013). A 27 day persistence model of near-Earth solar wind conditions: A long lead-time forecast and a benchmark for dynamical models. *Space Weather*, *11*(5), 225–236. doi: 10.1002/swe.20040
- Owens, M. J., Lang, M., Riley, P., Lockwood, M., & Lawless, A. S. (2020). Quantifying the latitudinal representivity of in situ solar wind observations. *Journal of Space Weather and Space Climate*, *10*. doi: 10.1051/swsc/2020009
- Owens, M. J., & Riley, P. (2017). Probabilistic Solar Wind Forecasting Using Large Ensembles of Near-Sun Conditions With a Simple One-Dimensional “Upwind” Scheme. *Space Weather*, *15*(11), 1461–1474. doi: 10.1002/2017SW001679
- Owens, M. J., Riley, P., Lang, M., & Lockwood, M. (2019). Near-Earth Solar Wind Forecasting Using Corotation From L5: The Error Introduced By Heliographic Latitude Offset. *Space Weather*, *17*(7), 1105–1113. Retrieved from

- 489 <https://doi.org/10.1029/2019SW002204> doi: 10.1029/2019SW002204  
490 Parker, E. N. U. o. C. (1958). Dynamics of the Interplanetary Gas and Magnetic  
491 Fields. *Astrophysical Journal*, 664 – 676. Retrieved from [https://sci-hub](https://sci-hub.tw/10.1002/iroh.19620470121)  
492 [.tw/10.1002/iroh.19620470121](https://sci-hub.tw/10.1002/iroh.19620470121)
- 493 Posner, A., Arge, C. N., Staub, J., StCyr, O. C., Folta, D., Solanki, S. K., ...  
494 Sterken, V. J. (2021). A Multi-Purpose Heliophysics L4 Mission. *Space*  
495 *Weather*, 19(9), 1–27. doi: 10.1029/2021SW002777
- 496 Richardson, I. G., & Cane, H. V. (2012). Solar wind drivers of geomagnetic storms  
497 during more than four solar cycles. *Journal of Space Weather and Space Cli-*  
498 *mate*, 2, 1–9. doi: 10.1051/swsc/2012001
- 499 Riley, P., Linker, J. A., & Arge, C. N. (2015). On the role played by magnetic ex-  
500 pansion factor in the prediction of solar wind speed. *Space Weather*, 13(3),  
501 154–169. doi: 10.1002/2014SW001144
- 502 Riley, P., Linker, J. A., & Mikić, Z. (2001). An empirically-driven global MHD  
503 model of the solar corona and inner heliosphere. *Journal of Geophysical Re-*  
504 *search: Space Physics*, 106(A8), 15889–15901. doi: 10.1029/2000ja000121
- 505 Riley, P., & Lionello, R. (2011). Mapping Solar Wind Streams from the Sun to 1  
506 AU: A Comparison of Techniques. *Solar Physics*, 270(2), 575–592. doi: 10  
507 .1007/s11207-011-9766-x
- 508 Simunac, K. D., Kistler, L. M., Galvin, A. B., Popecki, M. A., & Farrugia, C. J.  
509 (2009). In situ observations from STEREO/PLASTIC: A test for L5  
510 space weather monitors. *Annales Geophysicae*, 27(10), 3805–3809. doi:  
511 10.5194/angeo-27-3805-2009
- 512 Stone, E. C., Frandsen, A. M., & Mewaldt, R. A. (1998). The Advanced Composi-  
513 tion Explorer. *Space Science Reviews*, 86, 1–22. Retrieved from [https://doi](https://doi.org/10.1023/A:1005082526237)  
514 [.org/10.1023/A:1005082526237](https://doi.org/10.1023/A:1005082526237)
- 515 Thomas, S. R., Fazakerley, A., Wicks, R. T., & Green, L. (2018). Evaluating the  
516 Skill of Forecasts of the Near-Earth Solar Wind Using a Space Weather Moni-  
517 tor at L5. *Space Weather*, 16(7), 814–828. doi: 10.1029/2018SW001821
- 518 Tóth, G., Sokolov, I. V., Gombosi, T. I., Chesney, D. R., Clauer, C. R., De Zeeuw,  
519 D. L., ... Kóta, J. (2005). Space weather modeling framework: A new tool for  
520 the space science community. *Journal of Geophysical Research: Space Physics*,  
521 110(A12), 1–21. doi: 10.1029/2005JA011126
- 522 Turner, H., Owens, M. J., Lang, M. S., & Gonzi, S. (2021). The Influence of  
523 Spacecraft Latitudinal Offset on the Accuracy of Corotation Forecasts. *Space*  
524 *Weather*, 19(8), 1–15. doi: 10.1029/2021sw002802
- 525 Vokhmyanin, M. V., Stepanov, N. A., & Sergeev, V. A. (2019). On the Evaluation  
526 of Data Quality in the OMNI Interplanetary Magnetic Field Database. *Space*  
527 *Weather*, 17(3), 476–486. doi: 10.1029/2018SW002113
- 528 Webb, D. F., & Howard, T. A. (2012). Coronal mass ejections: Observations. *Living*  
529 *Reviews in Solar Physics*, 9. doi: 10.12942/lrsp-2012-3